photonics

MDPI

Article

Time-Resolved Calibration of Photon Detection Efficiency and Afterpulse Probability in 100 MHz Gated InGaAs/InP Single-Photon Avalanche Diodes

Zeyun Wang [1], Yiping Zhang [1], Hanqin Gu [1], Chao Han [1], Liang Yin [1] and Yan Liang [1,2,*]

[1] School of Optical-Electrical and Computer Engineering, University of Shanghai for Science and Technology, Shanghai 200093, China; 222180371@st.usst.edu.cn (Z.W.); 233350673@st.usst.edu.cn (Y.Z.); 2235061412@st.usst.edu.cn (H.G.); 223330748@st.usst.edu.cn (C.H.); yinliang@usst.edu.cn (L.Y.)
[2] Shanghai Research Center for Quantum Sciences, Shanghai 201215, China
* Correspondence: yanliang@usst.edu.cn

Abstract: InGaAs/InP single-photon avalanche diodes (SPADs) are widely used in applications such as quantum information, deep-space communication, and LiDAR. However, the existence of afterpulsing effects leads to inaccuracies in the calibration of their performance, particularly in terms of photon detection efficiency (PDE). In this paper, we employ the capacitance-balancing method to achieve a 100 MHz gated InGaAs/InP SPAD and propose a time-correlated calibration method to measure its performance. The distribution of the afterpulse counts over time is predicted, enabling a valid distinction between photogenerated counts and error counts. A PDE higher than ~30% is reached with an afterpulse probability of ~15%, while the repetition frequency of the incident laser (f_{laser}) changes from 1 MHz to 50 MHz. A comparison of the existing methodologies for calculating PDE reveals that PDE increases with f_{laser}. This increase is particularly pronounced when the PDE is high. However, under the time-correlated calibration scheme employed, the PDE remains almost constant, thereby validating the reliability of the results.

Keywords: single-photon avalanche diode; afterpulsing effect; InGaAs/InP APD

check for updates

Received: 15 April 2025
Revised: 19 May 2025
Accepted: 22 May 2025
Published: 24 May 2025

Citation: Wang, Z.; Zhang, Y.; Gu, H.; Han, C.; Yin, L.; Liang, Y. Time-Resolved Calibration of Photon Detection Efficiency and Afterpulse Probability in 100 MHz Gated InGaAs/InP Single-Photon Avalanche Diodes. *Photonics* **2025**, *12*, 534. https://doi.org/10.3390/photonics12060534

Copyright: © 2025 by the authors. Licensee MDPI, Basel, Switzerland. This article is an open access article distributed under the terms and conditions of the Creative Commons Attribution (CC BY) license (https://creativecommons.org/licenses/by/4.0/).

1. Introduction

Single-photon detectors (SPDs), which are devices that convert photon-level light signals into macroscopic electrical signals, are widely used in applications demanding sensitive light detection. In contrast to visible light detection, the extension of the spectral response of SPDs to the short-wave infrared (SWIR) region provides several significant advantages. These include enhanced compatibility with the low-loss fiber-optic communication window, improved eye safety, reduced background solar radiation, and increased atmospheric transmission through smoke-related obstacles [1,2]. InGaAs/InP single-photon avalanche photodiodes (InGaAs/InP SPADs) and superconducting nanowire single-photon detectors (SNSPDs) are two of the most used detectors in the SWIR. Generally, SNSPDs are favored for their high photon detection efficiency (PDE) > 90% and low error counts. However, SNSPDs need to work at cryogenic temperatures, which introduces complex systems and high costs [3]. In contrast, InGaAs/InP SPADs offer significant advantages in terms of operation at room temperature and system integration flexibility, making them the preferred detectors for many advanced photonic applications [4], such as LiDAR [5], quantum communication [6], and remote sensing [7].

The primary limitation of InGaAs/InP SPADs' performance is the afterpulsing effect. Afterpulses are transient error counts created by carriers trapped in material defects and

by delayed release. During an avalanche event, the current flowing through the diode fills some deep energy-level traps in the high-field multiplication region. These trapped carriers are later released after the defect-related lifetime. If these carriers are released during subsequent detection windows, they will contribute to excess counts. The release rate of carriers from traps is proportional to the number of occupied traps. This effect significantly limits the practical utility and performance of InGaAs/InP SPADs, as it not only reduces the photon counts but also increases the error counts [8]. Usually, tens to hundreds of nanoseconds of dead time must be introduced, resulting in a reduction in PDE and maximum count rate.

In recent years, significant progress has been made in mitigating the afterpulsing effect. One approach is to enhance the manufacturing process [9], minimizing the number of deep energy-level traps to reduce afterpulsing. Another approach focuses on circuit optimizations, limiting the charge carriers flowing during each avalanche pulse to further suppress afterpulsing. These studies focus primarily on hardware design improvements and operational strategies to reduce the afterpulsing effect. Theoretical research has also advanced, with Ripamonti et al. proposing a correction formula for the afterpulsing effects in idealized zero-dead-time detectors [10]. Subsequently, M. Höbel et al. introduced an efficient correction formula applicable to various detectors in multiphoton timing experiments to account for the combined effects of detector dead time and afterpulsing [11]. Lai et al. proposed a correction method based on a power-law model to analyze the probability distribution of afterpulsing effects [12]. Although the existing hardware improvements and operational strategies have reduced the afterpulsing effect to some extent, current methods still struggle to efficiently and accurately evaluate and quantify the specific impact of afterpulsing, particularly in high-speed gated InGaAs/InP SPADs. This has been observed to result in the overestimation of the total count rate, as well as a reduction in the duty cycle and PDE due to the increased dead times. In fluorescence microscopy, this phenomenon can result in an overestimation of the concentration of fluorophores [13]. In quantum communication, the overestimation of coincidence events increases the quantum bit error rate (QBER) [14]. Additionally, in laser ranging, the measurement of photon arrival times becomes significantly impaired [15]. Consequently, a comprehensive characterization of the afterpulse behavior could enhance the accuracy of various measurements in metrology.

In this study, we design a 100 MHz InGaAs/InP SPAD with ultrashort gates. The capacitance-balancing technique, which employs two cascading diodes to mimic the capacitive characteristic of the APD, is used to extract the avalanche signal with a spike noise rejection ratio of 14.5 dB. To evaluate the performance of this SPAD, a time-correlated single-photon counter (TCSPC) is employed to obtain the time-stamped SPAD output. While the repetition frequency of the incident pulsed laser (f_{laser}) varies from 1 MHz to 50 MHz, the detection efficiency can exceed 30%. However, the PDE is observed to increase with f_{laser} at the same bias voltage, suggesting inaccurate calibration. Thus, we propose a time-correlated calibration scheme that studies the time distribution of afterpulses based on their generation mechanism and analyzes the relationship between the normalized afterpulses and time to obtain a fitting function. With the scheme, the error counts, which include afterpulses and dark counts, can be effectively distinguished from the photogenerated counts. When the f_{laser} increases, the PDE remains almost constant. Compared with other commonly used calibration methods, the scheme we proposed gives more accurate results, ensuring the reliability of InGaAs/InP SPAD measurements in applications.

2. 100 MHz InGaAs/InP SPAD

Once the bias voltage (V_{bias}) superposed on the APD exceeds the avalanche breakdown voltage (V_{BR}), the APD enters Geiger mode, in which carriers generated by photon

absorption are gradually amplified by impact ionization, eventually forming a detectable macroscopic current. An external circuit is required to bring V_{bias} below V_{BR} to quench the avalanche and prepare for the next detection. An InGaAs/InP SPAD is typically operated in the gated Geiger mode, as shown in Figure 1b. The bias voltage (V_{bias}) applied to the APD consists of the DC voltage (V_{HV}) and the gating signals. When the gating signal is off, V_{bias} is lower than V_{BR} (V_{HV} is set to be lower than V_{BR}). The avalanche signal cannot be generated. On the contrary, when the gating signal is on, the APD enters the Geiger mode, which is capable of single-photon detection, as displayed in Figure 1a. With the gating signal, the afterpulses can be effectively suppressed, considering the condition that the trapped carriers are partly released when the gate is off. In addition, the average dark count rate of the gated SPAD is much lower than that observed in continuous operation mode, greatly improving the signal-to-noise ratio of the detection.

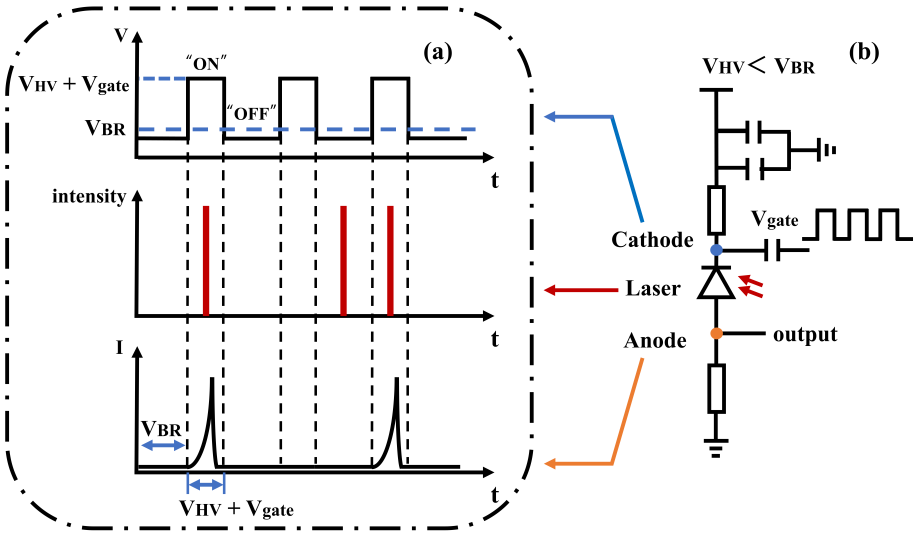


Figure 1. Diagram of (**a**) gated APD responding to laser pulses; (**b**) principle of gated APD.

In this experiment, we use ultrashort pulses with a full width at half maximum (FWHM) of ~0.95 ns as the gating signals of the APD. The repetition frequency of the gating signals is set to be 100 MHz. As exhibited in Figure 2a, the spike noise is be introduced as the gating signals charge and discharge on the APD. The capacitance-balancing method is employed to remove the spike noise and offers the advantages of low cost and high adaptability. Due to the APD's small capacitive characteristics, two cascaded Schottky diodes are needed to mimic these characteristics. As illustrated in Figure 2e, we connect the APD in parallel with the two diodes. The gating signal is divided into two equal parts, which are subsequently loaded onto the cathode of the APD and the diode, respectively. A magic-T network (MTNT) is utilized to subtract the signals from the APD and diode anode, thereby achieving suppression of the spike noise. A low-noise amplifier (AMP) is then placed after the MTNT to amplify the output signal with a gain of 20 dB. Furthermore, the DC bias voltage on the diodes (V_{Diode}) is adjusted by a variable resistor to finely tune their capacitive characteristics to perfectly match the spike noise. When we only connect the APD, the signal at point c is shown in Figure 2a and corresponds to the spike noise with an amplitude of 274.5 mV. In the opposite scenario, we connect only the diodes and observe a signal at point c with an amplitude of −275.7 mV, as shown in Figure 2b. Finally, when we connect both the APD and the diodes, the signal reaches an amplitude of 51.5 mV, as illustrated in Figure 2c. There is also a remaining noise signal due to the phase mismatch between the APD and the diode-generated signal. It is evident that the suppression of spike noise can be enhanced by implementing a more precise adjustment of the delay of

these two signals. Here, the employed capacitance-balancing method allows the spike noise suppression ratio to reach 14.5 dB, successfully separating the avalanche signal from the spike noise. Figure 2d shows an avalanche signal with an amplitude of ~183.8 mV. The extracted signal is then processed through a pulse-shaping circuit and converted into a digital output.

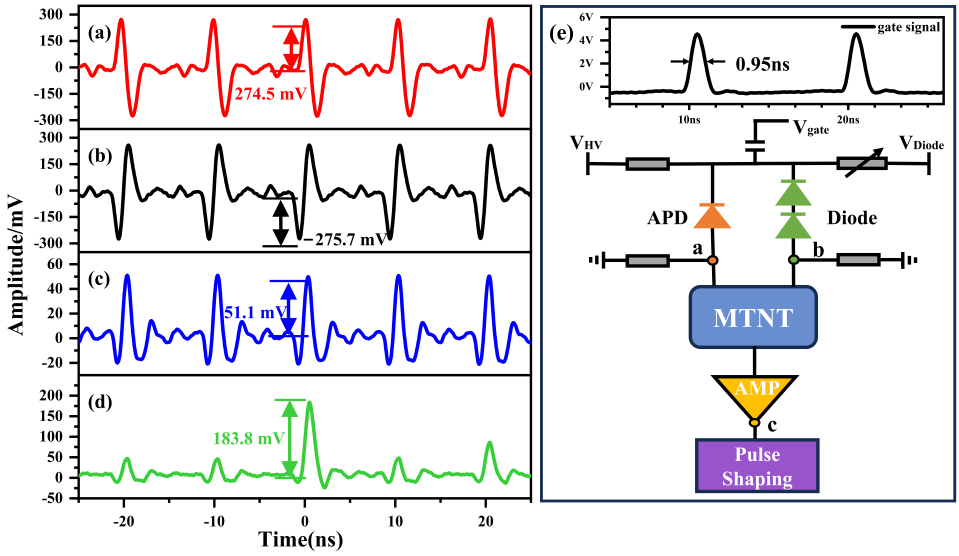


Figure 2. (**a**) APD-generated spike noise; (**b**) diode-stimulated spike noise; (**c**) differentially suppressed noise; (**d**) avalanche signal; (**e**) schematic of the capacitance-balancing circuit. Point a: output of the APD; Point b: the output of the diodes; Point c: output of the MTNT.

Based on the scheme in Figure 2e, we integrate the SPAD with modules, including a temperature controller, cooling box, gate generator, pulse-shaping unit, delay regulator, DC voltage setting, and FPGA. Through a USB interface connected to the computer, the FPGA serves as a core data processing component. The flowchart and physical picture of the InGaAs/InP SPAD-based detector are displayed in Figure 3a. The APD is cooled by a thermoelectric cooler to −50 °C to reduce its dark current. A temperature-control module is equipped with a high-precision thermistor and a fast negative feedback circuit, ensuring that the operation temperature of the APD does not vary more than 0.1 °C under different working conditions. Moreover, the capacitance-balancing circuit is placed in the cooling box to decrease the parasitic capacitance of the APD and electromagnetic interference from the environment. The gate generator module produces gating pulses triggered by the FPGA with a tunable repetition frequency from 1 to 200 MHz. The pulse width and V_{gate} are adjustable, while they remain the same at different gating repetition frequencies (f_{gate}). The DC voltage-setting module is used to change the V_{HV} with a resolution of 0.1 mV, guaranteeing the precise control of the avalanche gain of the APD. Finally, the avalanche signals are converted to digital signals by a pulse-shaping module and then sent to the FPGA to count the avalanches while outputting a synchronized digital signal.

To characterize the performance of the detector, we employ a home-made 1550 nm pulsed laser with a pulse width of ~50 ps as the incident light source, as displayed in Figure 3a. One output of the signal generator (SG) serves as the trigger for the laser, while the other functions as the trigger for the SPAD's gating signal. The delay between the two triggers can be adjusted by the delay regulator module of the detector with a resolution of 10 ps to optimize the PDE. In the system, we utilize a time-correlated single-photon counting (TCSPC) module (quTAG–Standard, qutools) to record the temporal characteristics of the detector's outputs. The TCSPC features a minimum timing jitter < 3.2 ps RMS, four channels, and a minimal time resolution of 1 ps. The TCSPC takes the synchronous signal

of the laser and the output of the detector as its "START" and "STOP" signals, respectively. The time resolution is set to be 100 ps, accounting for the TCSPC's maximum counts and the f_{laser}. Finally, the TCSPC records the avalanche events and provides the time stamps for each event, providing the data to calculate the PDE, afterpulse, and timing jitter for the overall assessment of the detector.

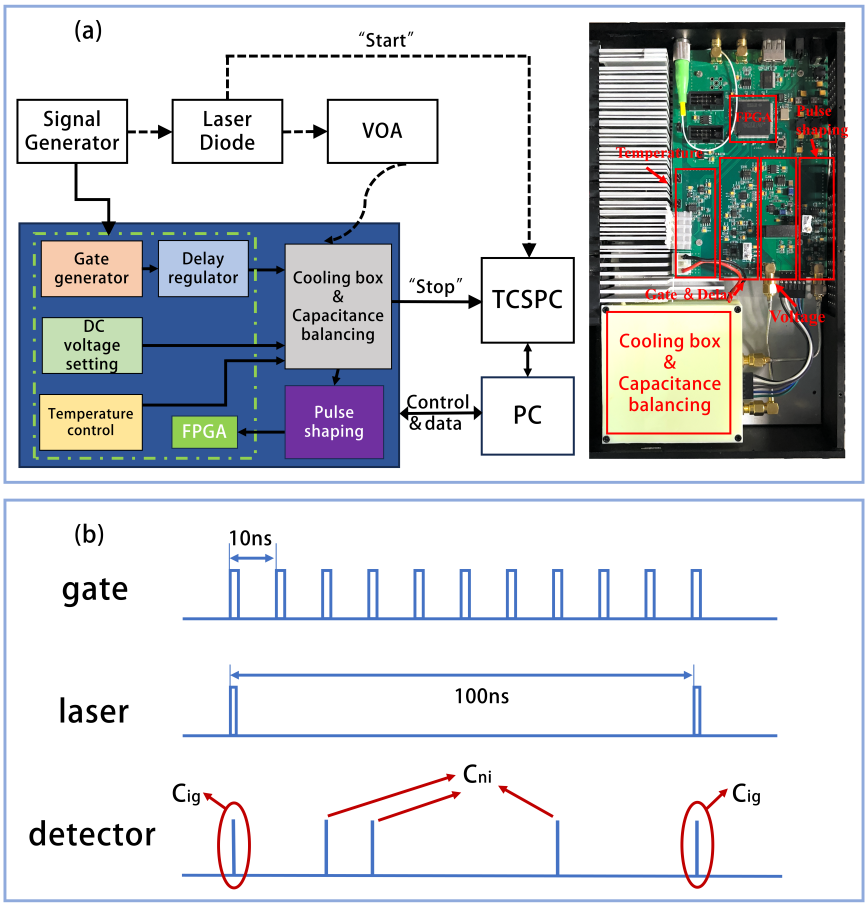


Figure 3. (**a**) Schematic of the experimental set-up; (**b**) temporal illustration of the laser pulses, the gating signals of the APD, and the output of the detector.

Here, we select f_{laser} values of 1 MHz, 2 MHz, 5 MHz, 10 MHz, 12.5 MHz, 20 MHz, 25 MHz, and 50 MHz to make sure that each laser pulse can be detected within the 100 MHz gating signal. Moreover, the laser is attenuated to contain an average photon number of 0.1 per pulse at different f_{laser} values before illuminating the APD. Considering the Poisson distribution of the photon numbers, the probability of multiphoton events is lower than 1%, allowing for an accurate assessment of the detector's performance. The gates corresponding to the laser pulses are referred to as illuminated gates, while the others are referred to as non-illuminated gates. Thus, the count rate in the illuminated gates and non-illuminated gates are defined as C_{ig} and C_{ni}, respectively, as displayed in Figure 3b. C_{ni} consists of the dark count rate and the afterpulses, while C_{ig} are usually regarded as the photon-induced count rate.

3. Experiments and Results

We measure the PDE, afterpulse probability, and dark count rate to characterize the detector. Typically, the PDE should be calculated considering the Poisson distribution and using the following formula [16]:

$$\eta = \frac{1}{\mu}\ln\left(\frac{1 - P_d}{1 - C_{ig}/f_{laser}}\right), \quad (1)$$

μ is the average photon number per laser pulse, and P_d is the dark count rate probability per gate, which is also one of the key parameters for the SPAD's performance. It can be expressed as shown in Formula (2):

$$P_d = \frac{C_{dcr}}{f_{gate}}, \quad (2)$$

C_{dcr} is the dark count rate corresponding to all gates. Meanwhile, C_{ni} can be obtained by subtracting C_{ig} from the total count rate $C_{t.}$ Usually, the afterpulsing count rate can be obtained by simply subtracting the dark count rate from C_{ni}. The non-illuminated gate afterpulse probability (P_{ap}) can then be calculated as the ratio of the afterpulsing count rate to C_{ig}, as in Formula (3) [17]:

$$P_{ap} = \frac{Ct - C_{ig} - C_{dcr}}{C_{ig}}, \quad (3)$$

Furthermore, the total count rate is quite important when considering the detector employed in specific applications, such as remote sensing, Raman spectroscopy, and biospectral imaging. We define the parameter R as the C_t-to-incident-photon ratio:

$$R = \frac{C_t}{\mu \times f_{laser}}, \quad (4)$$

First, we choose f_{laser} values of 1 MHz, 20 MHz, and 50 MHz to characterize the SPAD, as outlined in Table 1. The R grows steadily with a step of 5% by increasing the V_{HV} applied to the APD. Concurrently, the dark count rate increases slowly with the SPAD's total count rate. Compared with the afterpulses, the dark counts can almost be ignored. With the increase in R, the calculated PDE (η) and P_{ap}, which follow Formulas (1) and (3), increase. The increase in PDE slows down, especially once R exceeds 35%. In contrast, the P_{ap} rises significantly. For instance, the PDE increases slightly from 32.6% to 33.6% with R increasing from 40% to 45% at f_{laser} = 1 MHz, while P_{ap} increases from 25.1% to 35.5%. It can be deduced that P_{ap} is a key parameter that limits the maximum PDE of the InGaAs/InP SPAD.

Table 1. Calculated PDE (η) following Formula (1) and P_{ap} following Formula (3) as a function of R at f_{laser} values of 1 MHz, 20 MHz, and 50 MHz.

f_{laser} (Hz)	R (%)	η (%)	P_{ap} (%)	P_d ($\times 10^{-7}$)
1 M	25	24.8	3.3	7.9
	30	28.8	6.4	11.8
	35	31.4	13.2	16.2
	40	32.6	25.1	22.1
	45	33.6	35.5	27.1
20 M	25	24.7	3.2	10.1
	30	28.5	7.0	15.0
	35	31.4	13.1	21.1
	40	33.0	22.4	27.3
	45	34.8	30.3	42.3
50 M	25	25.2	1.6	12.1
	30	29.8	3.6	17.3
	35	33.3	7.0	24.0
	40	36.7	11.4	33.0
	45	39.6	15.7	67.8

Furthermore, we observe that the PDEs are almost the same at f_{laser} values of 1 MHz and 20 MHz, while the PDEs are higher at 50 MHz. For example, if R = 40%, the PDE is 32.6% at 1 MHz and 33.0% at 20 MHz, whereas at 50 MHz, it is calculated to be 36.7%. As for P_{ap}, the trend seems to be the opposite. P_{ap} is much lower at 50 MHz than at 1 MHz. At a 50 MHz f_{laser}, P_{ap} is measured to be 15.7% at an R of 45%, while reaching 35.5% at 1 MHz. If R is less than 35%, the variation between the P_{ap} values at 1 MHz and 20 MHz is minimal. However, if R exceeds 40%, the P_{ap} values at 20 MHz become lower than those at 1 MHz. During the experiment, to obtain the same value of R at the three different f_{laser} values, V_{HV} is set at almost the same value. Theoretically, the PDEs should be identical at 1 MHz, 20 MHz, and 50 MHz, as should the P_{ap} values. Thus, we believe that the methods of calculating PDE and P_{ap} should be appropriately modified to meet the needs of high-speed detection.

To address the issue of the inaccurate calibration of the SPAD, we study the time distribution of the detector's output counts. Figure 4a and Figure 4b show the distributions of counts obtained by the TCSPC for R = 40% at 1 MHz and 10 MHz f_{laser} values, respectively. The first counting peak represents the photogenerated counts, while the subsequent peaks correspond to the error counts, which consist mainly of afterpulses. Since the first peak is much higher than the others, we show the distributions of the error counts in the inset of Figure 4a,b in detail. The change in error counts is more pronounced at 1 MHz than at 10 MHz, suggesting a fuller release of the afterpulses during this period. The peak value of the error counts drops from 230 to 7 at 1 MHz, while it decreases from ~3200 to 1180 at 10 MHz. Moreover, we present the error counts at 100 ns intervals in Figure 4a for comparison. It can be observed that the proportion of counts in the first 100 ns interval constitutes 52.0% of the aggregate count, while it declines sharply to 14.2% in the second interval, and then the percentages in the subsequent intervals decrease gradually. In the fifth interval, the proportion decreases to 4.7%, while in the last interval, it is calculated to be 0.2%. We believe that when f_{laser} = 1 MHz, more than 99% of the afterpulsing counts can be counted, allowing both the PDE and P_{ap} to be prepared for calibration. However, when f_{laser} = 10 MHz, only ~50% of the afterpulses are released in the 100 ns laser cycle, and the rest are likely to be released in subsequent illuminated gates, i.e., counted as photogenerated counts, leading to inaccurate calculation.

According to the statements in Ref. [18], the power-law dependence is consistent with the notion of a dense spectrum of trap levels and explains why both exponential and power-law behaviors are observed in the afterpulse release curve. To precisely determine the afterpulse count rate, we deduct the dark count rate that is recorded with the laser switched off. Furthermore, we determine the counts of each counting peak in non-illuminated gates to reduce the influence of the timing jitter of the SPAD on the temporal distribution of the afterpulses. As shown in Figure 4c,d, the normalized afterpulses per gate, which are obtained by dividing by the total accumulating afterpulses, decrease with time. Here, we assume the afterpulses follow a power-law dependence of time and fit the data with the following formula:

$$C_{nor,ap} = A(T \times f_{gate})^{-\alpha}, \quad (5)$$

T is defined as $(10\ N + 5) \times 10^{-9}$ s, where N is the Nth non-illuminated gate after the illuminated gate. Here, N should be greater than 2, considering the dead time of the detector is ~13 ns. α is an effective decay constant, and A is the pre-factor. By fitting the data with time, we extract the corresponding values of A and α. As displayed in Figure 4c, A = 0.435 and $\alpha = -1.22$ are found to exhibit the best fit when f_{laser} = 1 MHz. The fitted curve in red and the data points in blue exhibit a high degree of overlap. At f_{laser} = 10 MHz, the corresponding values of A and α are 0.418 and -0.78, respectively, as shown in Figure 4d. The fitted curve also fits the data points well. Hence, we can predict

the afterpulses in the illuminated gate (C_{iap}) as well. The yellow square point in Figure 4d is regarded as the number of normalized afterpulses in the illuminated gate ($C_{nor,iap}$). As previously mentioned, the afterpulses are not fully released during the 100 ns laser cycle, which results in the inaccurate calibration of the PDE and P_{ap}. The utilization of predicted values is demonstrated to resolve this issue. By subtracting C_{iap} from the illuminated gate counts and adding it to the non-illuminated gate counts, we propose two formulas to calculate the PDE and P_{ap} that correspond to all gates.

$$PDE = \frac{1}{\mu}\ln\left(\frac{1 - P_d}{1 - (C_{ig} - C_{iap})/f_{laser}}\right), \quad (6)$$

$$P_{ap} = \frac{C_{ni} + C_{iap} - C_{dcr}}{C_{ig} - C_{iap}}, \quad (7)$$

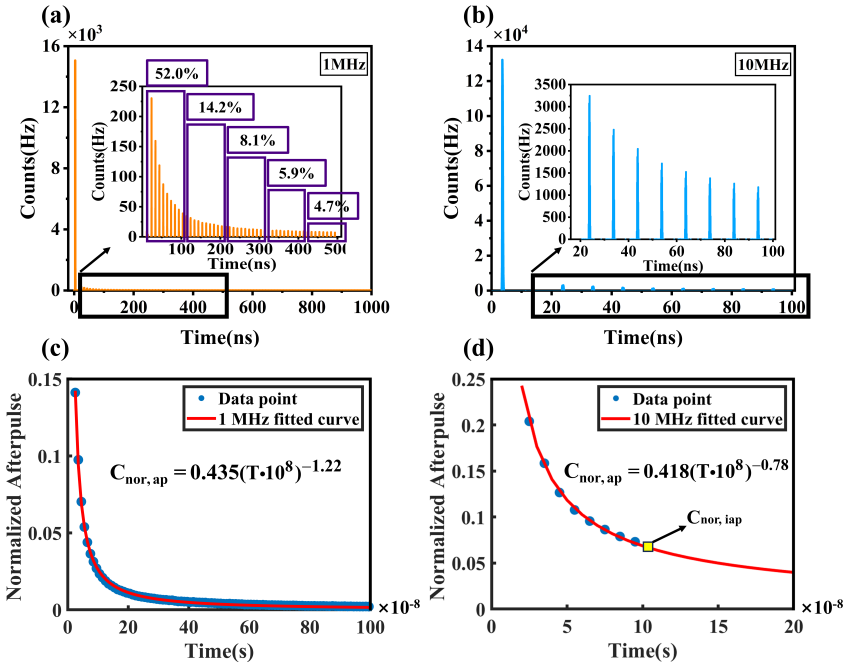


Figure 4. R = 40%, μ = 0.1, avalanche distribution over time at (**a**) f_{laser} = 1 MHz, (**b**) f_{laser} = 10 MHz; (**c**) data points and fitted curve at f_{laser} = 1 MHz; (**d**) data points and fitted curve at f_{laser} = 10 MHz. The yellow square point is the predicted number of normalized afterpulses in the illuminated gate.

Varying the f_{laser} from 1 MHz to 50 MHz, we use Formulas (1) and (3) to calculate the PDE and P_{ap} when R is set at 20% and 40%, respectively. Meanwhile, we employ Formulas (6) and (7) for comparison. If f_{laser} is below 25 MHz, C_{iap} can be obtained through curve fitting. However, when f_{laser} = 50 MHz, the 100 MHz gating test provides only a single data point for the non-illuminated gate, which is insufficient for us to fit. Here, we directly regard the recorded afterpulses in the only non-illuminated gate as C_{iap} for this case. Figure 5a illustrates the case when R = 20%; the P_{ap} at f_{laser} = 1 MHz is 1.85% and decreases gradually with the increase in f_{laser}, while the PDE remains nearly constant. In this condition, the P_{ap} is relatively low, and its impact on PDE is negligible. However, when R = 40%, as shown in Figure 5b, the P_{ap} falls from 25.1% to 11.4%, showing a more pronounced decreasing trend. The afterpulsing effect at this point becomes significant enough to influence the PDE, causing it to gradually rise from 32.6% to 36.7%. The corresponding results with our proposed formulas are shown in Figure 5c for R = 20% and Figure 5d for R = 40%, where both the PDE and P_{ap} are optimized. The P_{ap} fluctuates slightly around 1.8% at R = 20%, with a maximum value of 2.0% and a minimum value of 1.7%. The effect

of the correction is more remarkable at R = 40%, with a P_{ap} of ~28%, where the maximum and minimum values of P_{ap} are recorded as 28.2% and 24.2%, respectively. Meanwhile, the calculated PDE no longer shows a clear upward trend with increasing f_{laser} as in Figure 5b but floats slightly around 32.0%. For instance, when f_{laser} = 50 MHz, the proposed formula corrects the PDE from 36.7% to 32.4%, while a further enhancement is observed in P_{ap} from 11.4% to 25.6%. In general, both the PDE and P_{ap} corrected by our time-correct method remain approximately constant at different f_{laser} values. This validates the effectiveness of the proposed scheme.

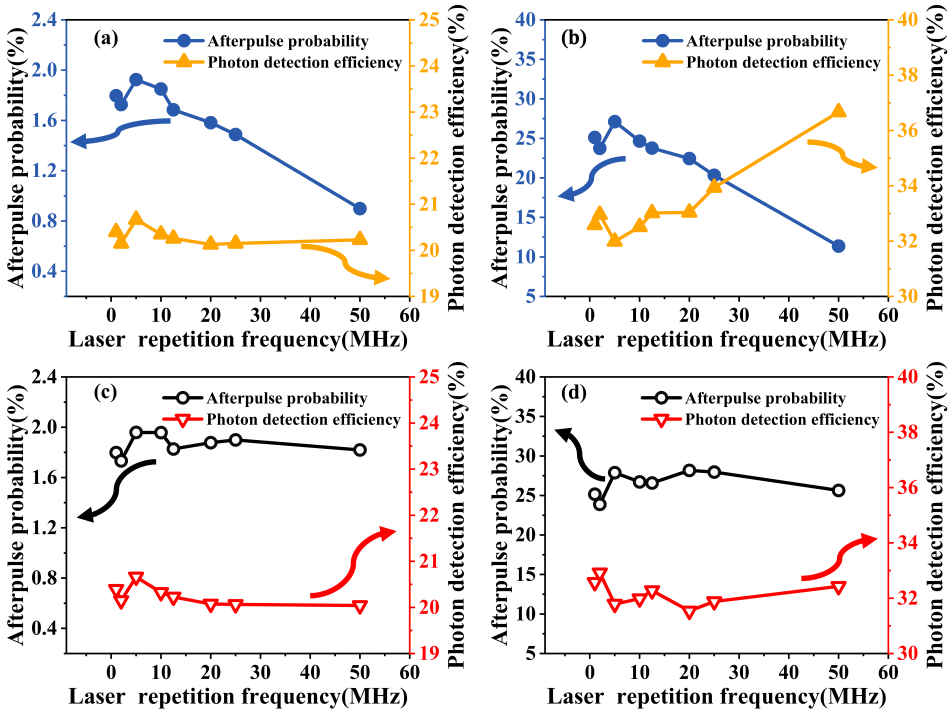


Figure 5. Calculated P_{ap} and PDE values upon varying the f_{laser} from 1 MHz to 50 MHz. The PDE and P_{ap} are calculated using Formulas (1) and (3), respectively, at (**a**) R = 20% and (**b**) R = 40%; the PDE and P_{ap} are calculated using Formulas (6) and (7), respectively, at (**c**) R = 20% and (**d**) R = 40%.

To demonstrate the correction effect of our method at different afterpulses in detail, we compare the PDEs calculated by Formula (1) and Formula (6) at the different R values while f_{laser} ranges from 1 MHz to 50 MHz. The value of R increases steadily in steps of 5% and is set at 25%, 30%, 35%, and 40%. As displayed in Figure 6, the step of increase in PDE is not as consistent as that of R. As R increases, the increase in PDE becomes smaller. This phenomenon can be attributed to the rise in the afterpulses. With Formula (1), as R increases from 25% to 40%, the difference between the calculated PDEs becomes more pronounced at varying f_{laser} values, particularly when R exceeds 35% and f_{laser} surpasses 20 MHz. In contrast, the employment of our proposed Formula (6) ensures that the PDEs remain relatively constant across varying f_{laser} values at diverse R values. When R = 25%, the two curves almost overlap each other. For instance, when f_{laser} = 25 MHz, the PDE obtained with Formula (1) is 24.7%, while that for Formula (6) is 24.5%. However, if R = 35%, when f_{laser} = 50 MHz, the PDE obtained with Formula (1) is 33.3%, with a value of 30.9% for Formula (6). Conversely, when f_{laser} = 10 MHz, the PDE for Formula (1) is 30.9%, with a value of 30.6% for Formula (6). It can be concluded that the PDE can be precisely calculated with our method by effectively reducing the influence of afterpulses. Additionally, the reliability of this method is enhanced for the detectors of high P_{ap} values.

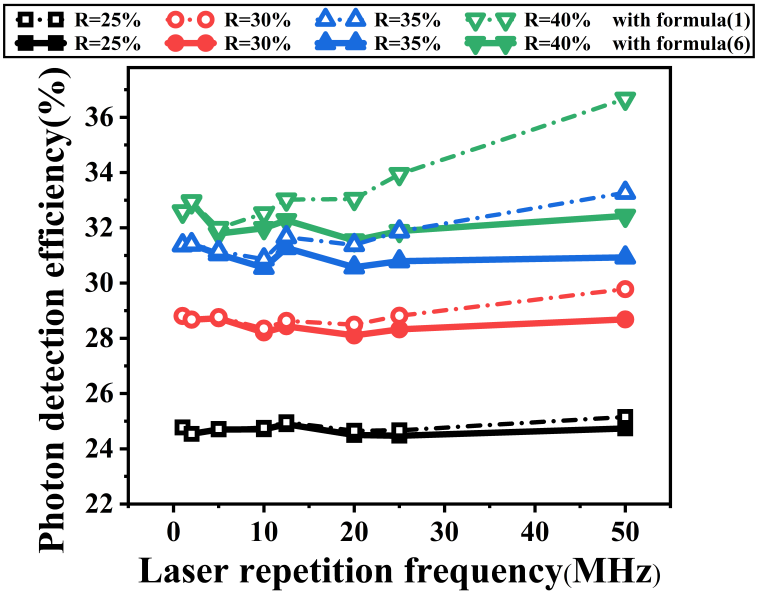


Figure 6. Comparison of PDEs obtained using Formula (1), shown with a dotted line, and Formula (6), shown with a solid line, when R is set at 25%, 30%, 35%, and 40%.

There are several widely used methods for determining afterpulse probability, such as the Bethune method (Equation (1)) [17], Yuan's method [19], the double-pulse method [20,21], the autocorrelation method [22], and the Klyshko method [23,24]. However, the double-pulse method is only applicable to SPADs gated with short pulses and requires the gating interval to be adjustable. The autocorrelation method requires multi-channel autocorrelator devices. The Klyshko method is designed for true single-photon sources based on parametric down-conversion effects, which are not applicable to attenuated lasers with multiphoton states. Yuan's method, which is used most often, determines the afterpulses per gate by averaging the afterpulses in non-illuminated gates, while our method obtains the afterpulses by fitting the time distribution of afterpulses. Thus, our approach offers better accuracy and broader applicability for high-speed single-photon detection.

4. Conclusions

In summary, we present a 100 MHz ultrashort-gated InGaAs/InP SPAD, which mainly consists of several modules, including temperature control, a cooling box, a gate generator, pulse shaping, a delay regulator, DC voltage setting, and an FPGA in charge of sending and receiving data. The capacitance-balancing method, which employs two cascading diodes to mimic the capacitance of the APD, is used to obtain a spike noise suppression ratio of 14.5 dB. A time-correlated calibration scheme, which can predict the afterpulses by fitting the afterpulse distribution over time, is demonstrated to distinguish between the photogenerated counts and the afterpulses. Two calculation formulas are proposed to accurately calibrate the PDE and P_{ap}. As f_{laser} changes from 1 MHz to 50 MHz, the values of PDE almost remain constant. Furthermore, with an increase in afterpulse probability, the correction effect of our scheme is more pronounced compared to that obtained with the previously proposed method. Therefore, it can be concluded that our method is applicable for high-speed contexts, especially for GHz InGaAs/InP single-photon detectors.

Author Contributions: Methodology, Y.L.; investigation, Y.Z. and H.G.; validation, Z.W. and C.H.; writing—original draft preparation, Z.W. and L.Y.; writing—review and editing, Y.L. All authors have read and agreed to the published version of the manuscript.

Funding: This research was funded by the Innovation Program for Quantum Science and Technology (2023ZD0301000), National Natural Science Foundation of China (62175152), and Shanghai Municipal Science and Technology Major Project (2019SHZDZX01).

Institutional Review Board Statement: Not applicable.

Informed Consent Statement: Not applicable.

Data Availability Statement: Data are contained within the article.

Conflicts of Interest: The authors declare no conflicts of interest.

References

1. Vines, P.; Kuzmenko, K.; Kirdoda, J.; Dumas, D.C.S.; Mirza, M.M.; Millar, R.W.; Paul, D.J.; Buller, G.S. High performance planar germanium-on-silicon single-photon avalanche diode detectors. *Nat. Commun.* **2019**, *10*, 1086. [CrossRef] [PubMed]
2. Cai, Y.; Chen, Y.; Dorfman, K.; Xin, X.; Wang, X.; Huang, K.; Wu, E. Mid-infrared single-photon upconversion spectroscopy enabled by nonlocal wavelength-to-time mapping. *Sci. Adv.* **2024**, *10*, eadl3503. [CrossRef] [PubMed]
3. Zhou, H.; He, Y.-H.; Lü, C.-L.; You, L.-X.; Li, Z.-H.; Wu, G.; Zhang, W.-J.; Zhang, L.; Liu, X.-Y.; Yang, X.-Y.; et al. Photon-counting chirped amplitude modulation lidar system using superconducting nanowire single-photon detector at 1550-nm wavelength. *Chin. Phys. B* **2018**, *27*, 018501. [CrossRef]
4. Gol'tsman, G.N.; Okunev, O.; Chulkova, G.; Lipatov, A.; Semenov, A.; Smirnov, K.; Voronov, B.; Dzardanov, A.; Williams, C.; Sobolewski, R. Picosecond superconducting single-photon optical detector. *Appl. Phys. Lett.* **2001**, *79*, 705–707. [CrossRef]
5. Zhu, X.; Wang, Y.; Li, Z.; Li, X.; Wu, G. Two-Way Single-Photon Laser Time Transfer for High-Speed Moving Platforms. *Photonics* **2024**, *11*, 1028. [CrossRef]
6. Walker, T.; Miyanishi, K.; Ikuta, R.; Takahashi, H.; Kashanian, S.V.; Tsujimoto, Y.; Hayasaka, K.; Yamamoto, T.; Imoto, N.; Keller, M. Long-Distance Single Photon Transmission from a Trapped Ion via Quantum Frequency Conversion. *Phys. Rev. Lett.* **2018**, *120*, 203601. [CrossRef]
7. Gibson, S.J.; van Kasteren, B.; Tekcan, B.; Cui, Y.; van Dam, D.; Haverkort, J.E.M.; Bakkers, E.P.A.M.; Reimer, M.E. Tapered InP nanowire arrays for efficient broadband high-speed single-photon detection. *Nat. Nanotechnol.* **2019**, *14*, 473–479. [CrossRef]
8. Tosi, A.; Mora, A.D.; Zappa, F.; Cova, S. Single-photon avalanche diodes for the near-infrared range: Detector and circuit issues. *J. Mod. Opt.* **2009**, *56*, 299–308. [CrossRef]
9. Ke, S.; Chen, Z.; Zhou, J.; Jiao, J.; Chen, X.; Chen, S. Theoretical Prediction of High-Performance Room-Temperature InGaAs/Si Single-Photon Avalanche Diode Fabricated by Semiconductor Interlayer Bonding. *IEEE Trans. Electron Devices* **2021**, *68*, 1694–1701. [CrossRef]
10. Ripamonti, G.; Zappa, F.; Cova, S.D. Effects of trap levels in single-photon optical time-domain reflectometry: Evaluation and correction. *J. Light. Technol.* **1992**, *10*, 1398–1402. [CrossRef]
11. Hobel, M.; Ricka, J. Dead-time and afterpulsing correction in multiphoton timing with nonideal detectors. *Rev. Sci. Instrum.* **1994**, *65*, 2326–2336. [CrossRef]
12. Lai, Y.; Shen, Z.; Chen, Y.; Wang, J.; Guo, J.; Wei, Z. The Impact of Afterpulsing Effects in Single-Photon Detectors on the Performance Metrics of Single-Photon Detection Systems. *Photonics* **2024**, *11*, 1074. [CrossRef]
13. Ju, Z.; He, M.; Lin, J.; Zhu, J.; Wu, B.; Wu, E. High-resolution two-photon fluorescence microscope imaging of nanodiamonds containing NV color centers. *Results Phys.* **2022**, *40*, 105874. [CrossRef]
14. Stucki, D.; Gisin, N.; Guinnard, O.; Ribordy, G.; Zbinden, H. Quantum key distribution over 67 km with a plug&play system. *New J. Phys.* **2002**, *4*, 41. [CrossRef]
15. Xie, H.; Wang, Z.; Zhou, T.; Yang, K.; Liu, X.; Fu, Q.; Zhang, D.; Deng, M. Afterpulse correction for micro-pulse lidar to improve middle and upper tropospheric aerosol measurements. *Opt. Express* **2021**, *29*, 43502–43515. [CrossRef]
16. Campbell, J.C.; Sun, W.; Lu, Z.; Itzler, M.A.; Jiang, X. Common-Mode Cancellation in Sinusoidal Gating With Balanced InGaAs/InP Single Photon Avalanche Diodes. *IEEE J. Quantum Electron.* **2012**, *48*, 1505–1511. [CrossRef]
17. Bethune, D.S.; Risk, W.P.; Pabst, G.W. A high-performance integrated single-photon detector for telecom wavelengths. *J. Mod. Opt.* **2004**, *51*, 1359–1368. [CrossRef]
18. Korzh, B.; Lunghi, T.; Kuzmenko, K.; Boso, G.; Zbinden, H. Afterpulsing studies of low-noise InGaAs/InP single-photon negative-feedback avalanche diodes. *J. Mod. Opt.* **2015**, *62*, 1151–1157. [CrossRef]
19. Yuan, Z.L.; Kardynal, B.E.; Sharpe, A.W.; Shields, A.J. High speed single photon detection in the near infrared. *Appl. Phys. Lett.* **2007**, *91*, 041114. [CrossRef]
20. Zhang, J.; Thew, R.; Gautier, J.D.; Gisin, N.; Zbinden, H. Comprehensive Characterization of InGaAs-InP Avalanche Photodiodes at 1550 nm With an Active Quenching ASIC. *IEEE J. Quantum Electron.* **2009**, *45*, 792–799. [CrossRef]

21. Restelli, A.; Bienfang, J.C.; Migdall, A.L. Time-domain measurements of afterpulsing in InGaAs/InP SPAD gated with sub-nanosecond pulses. *J. Mod. Opt.* **2012**, *59*, 1465–1471. [CrossRef]
22. Arahira, S.; Murai, H. Effects of afterpulse events on performance of entanglement-based quantum key distribution system. *Jpn. J. Appl. Phys.* **2016**, *55*, 032801. [CrossRef]
23. Polyakov, S.V.; Migdall, A.L. High accuracy verification of a correlated-photon-based method for determining photoncounting detection efficiency. *Opt. Express* **2007**, *15*, 1390–1407. [CrossRef] [PubMed]
24. Klyshko, D.N. Use of two-photon light for absolute calibration of photoelectric detectors. *Sov. J. Quantum Electron.* **1980**, *10*, 1112–1116. [CrossRef]

Disclaimer/Publisher's Note: The statements, opinions and data contained in all publications are solely those of the individual author(s) and contributor(s) and not of MDPI and/or the editor(s). MDPI and/or the editor(s) disclaim responsibility for any injury to people or property resulting from any ideas, methods, instructions or products referred to in the content.